Garnet Electrolytes for Solid State Batteries: Visualisation of Moisture-Induced Chemical Degradation and Revealing its Impact on the Li-Ion Dynamics.

Rowena H. Brugge, A. K. Ola Hekselman, Andrea Cavallaro, Federico M. Pesci, Richard J. Chater, John A. Kilner and Ainara Aguadero*

Department of Materials, Imperial College London, Exhibition Road, SW7 2AZ, London, UK

ABSTRACT: In this work, we reveal the impact of moisture-induced chemical degradation and proton-lithium exchange on the Li-ion dynamics in the bulk, the grain boundaries and at the interface with lithium metal in highly Li-conducting garnet electrolytes. A direct correlation between chemical changes as measured by depth-resolved secondary ion mass spectrometry and the change in transport properties of the electrolyte is provided. In order to probe the intrinsic effect of the exchange on the lithium kinetics within the garnet structure, isolated from secondary corrosion product contributions, controlled-atmosphere processing was first used to produce proton-free $Li_{6.55}Ga_{0.15}La_3Zr_2O_{12}$ (Ga0.15-LLZO), followed by degradation steps in a H_2O bath at 100 °C, leading to the removal of LiOH secondary phases at the surface. The proton-exchanged region was analysed by focussed ion beam - secondary ion mass spectrometry (FIB-SIMS) and

found to extend as far as 1.35 μm into the Ga0.15-LLZO garnet pellet after 30 minutes in H_2O. Impedance analysis in symmetrical cells with Li metal electrodes evidenced a greater reactivity in grain boundaries than in grains and a significantly detrimental effect on the Li transfer kinetics in the Li metal/garnet interface correlated to a threefold decrease in the Li mobility in the protonated garnet. This result evidences that the deterioration of Li charge transfer and diffusion kinetics in proton-containing garnet electrolytes have fundamental implications for the optimisation and integration of these systems in commercial battery devices.

1. Introduction

Solid state inorganic electrolytes are fundamental for the development of the next generation of Li-metal batteries which are based on an all-solid-state framework. One major challenge for all-solid-state batteries is to provide an electrolyte with high room temperature Li conductivity, σ_{Li} >10^{-4} S cm^{-1}, in order to fulfil high power and fast recharging targets. The garnet-type electrolytes based on $Li_7La_3Zr_2O_{12}$ (LLZO) structures are amongst the most promising candidates in this respect, with reported conductivities greater than 1 mS cm^{-1} at room temperature in the Ga- doped cubic material[1–4], and compatibility with lithium metal anodes[5,6]. Ga-doped LLZO is thus used as a model system for this work since it is potentially suitable for the development of high energy density cells if problems with high interfacial resistance and dendritic-driven cell failure can be solved[7,8]. Understanding and controlling these problems is essential in order to enable the realisation of a next generation of energy storage technology with higher energy and power density, better safety features and longer cycle life than current Li ion cells.

Unfortunately, these fast Li-conductors display high reactivity with moisture leading to proton-lithium (H^+/Li^+) exchange in the bulk crystal structure of the garnet[9,10]. The existence of hydrogarnets obtained from proton exchange of anhydrous garnets (e.g. $Ca_3Al_2(OH)_{12}$ from

$Ca_3Al_2Si_3O_{12}$) has been known for some time[11], illustrating the ability for protons to successfully occupy O_4H_4 units around octahedral 96*h* sites in the cubic *Ia*$\bar{3}$*d* space group, whilst maintaining the crystal structure[12,13]. Several groups have used diffraction studies to evaluate the chemical stability and proton exchange of Li-stuffed garnets in water and air; provided the Li stoichiometry is greater than 3 atoms per formula unit, it has been shown that the exchange occurs readily[14]. Early studies showed that treatment of tetragonal Li garnet powders in water or acid resulted in the transformation to the cubic polymorph, a direct result of creating disorder in the Li network through H^+/Li^+ exchange[14–16]. Protonation of Li garnets with *Ia*$\bar{3}$*d* space group in air, water and acidic media has been reported; in many cases the cubic crystal structure is maintained[12,17], but some authors report a change in symmetry to a non-centrosymmetric *I*$\bar{4}$3*d* or *I*2$_1$3 space group[13,18,19]. In the cases where a change in symmetry is reported, powders of the Li-rich garnet are treated at high (>150 °C) and/or aged in air prior to characterisation, further complicating the picture.

The effect of the H^+/Li^+ exchange on the transport properties of the garnets is less widely reported, as most studies have focused on evaluating the powdered material. Simonishi *et al.* reported no change in bulk conductivity in LLZO pellets immersed in H_2O at 50 °C, but a decrease in the grain boundary conductivity[17]. Xia *et al.*[20] reported a reduction in total conductivity in Ta-doped LLZO pellets immersed in room temperature H_2O and predict a reduced Li^+ mobility in the protonated phase.

In addition to the exchange in the lattice, the process is accompanied by the formation of passivating Li hydroxide at the surface which transforms to carbonates when exposed to air[21]. This surface reactivity can severely compromise densification of the electrolyte into pellets, due to the formation of core-shell structures in the powder comprising of a Li garnet core, surrounded by a

3

proton-rich garnet shell and a $LiOH/Li_2CO_3$ outer layer[22]. The interfacial properties with lithium metal electrodes are also affected due to the formation of the $LiOH/Li_2CO_3$ degradation products on the surface of the ceramic[23], resulting in an increased interfacial resistance[24,25].

The formation of a proton-rich garnet together with the subsequent drop in Li charge carriers is likely to result in changes in the Li mobility and conduction mechanism[26] in the garnet lattice and at the grain boundaries in the pellet material; however, there have been a limited number of experimental studies of these phenomena, especially with regard to the impact on the charge transfer at the interface with lithium metal electrodes. The interplay between Li^+ and H^+ transport is fundamental to understand and optimise the Li transfer kinetics in all-solid-state batteries to allow reliable commercialisation of these devices. In this work, the role of the formation of a protonated LLZO pellet on the Li mobility in the grains, grain boundaries and interface with Li metal in Ga-doped LLZO is systematically investigated. We use controlled-atmosphere processing (using a glove box coupled to a high temperature furnace) to produce initially 'dry' pristine garnet pellets and subsequently promote H^+/Li^+ exchange in the lattice by controlled exposure to H_2O at 100°C. This step was chosen to remove water-soluble secondary LiOH phases known to form at the surface prior to analysis, thus isolating the effects of the ion exchange on the ion dynamics, and to probe macroscopically the associated chemical and transport processes by promoting a large and 'quantifiable' zone of ion exchange. We use low energy ion scattering (LEIS) and focussed ion beam - secondary ion mass spectrometry (FIB-SIMS) in combination with electrochemical impedance analysis to correlate local chemical features to variations in the ion dynamics of the surface, grains and grain boundaries.

2. Results and Discussion

2.1. Pristine Ga0.15-LLZO Characterisation

Pellets of Ga0.15-LLZO (nominal composition $Li_{6.55}Ga_{0.15}La_3Zr_2O_{12}$) of relative densities > 90 % as obtained by geometrical calculations measuring 8 mm diameter by 1 mm thickness were prepared via a sol-gel method (details in the Experimental Section). The resultant XRD pattern shows a cubic phase, with the space group $Ia\bar{3}d$, with a slight amount of Li_2ZrO_3 secondary phase (Figure S1a).

Grain boundaries and grain morphology can be revealed on thermal treatment of the pellet at 900 °C for 30 minutes, with the secondary electron image (Figure S1b) showing a bimodal distribution of grain sizes, some up to 20 μm diameter, others in the order of a few micrometres. The grain boundaries appear to be composed of a secondary phase which is expected to be amorphous as it is not detected by XRD, and are likely to be formed as a result of liquid-phase sintering of the pellet, a process which has been observed by other groups[23,27].

The FIB-SIMS instrument used in this study has the advantage of selected area analysis by high resolution secondary electron and ion imaging of the sample, large depth probing to several micrometres and simultaneous dual-polarity secondary ion detection[28]. By using small analysis crater sizes (7 μm by 7 μm) in the FIB-SIMS instrument we are thus able to select areas within the larger grains of Ga0.15-LLZO. Electrochemical impedance spectroscopy (EIS) was performed on the pristine Ga0.15-LLZO pellet with symmetrical lithium electrodes to determine ionic conductivity and charge transfer resistance. Figure 1 shows a Nyquist plot recorded at 25 ˚C, comprising an incomplete semicircle in the high-frequency region, followed by two depressed semicircles in the medium and the low frequencies.
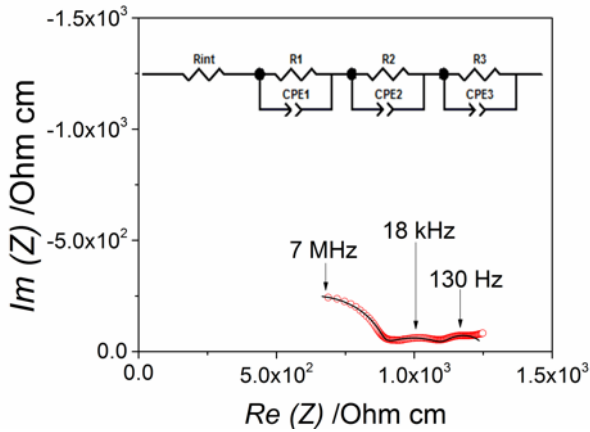
Figure 1. Impedance spectrum of a pristine Ga0.15-LLZO pellet in a symmetrical cell with lithium electrodes at 25 °C and an equivalent circuit used to fit the data. Open circles represent experimental data and the full line is the corresponding simulated fit. Impedance values are corrected by the sample geometry.

The data were fitted with a series of three parallel combinations of R//CPE circuits, where R corresponds to an ohmic resistor and CPE to a constant-phase element. An additional resistance element (R_{int}) in series was also included to account for inductive effects, resulting in the deformation of the high frequency semicircle. In this work, we found that the resistance corresponding to the system wiring was 5 Ω at room temperature. Geometrically-corrected capacitance and ionic conductivity values extracted from the fitted high frequency semicircle were 3.7×10^{-11} F cm^{-1} and 1.2×10^{-3} S cm^{-1}, respectively. This relatively low capacitance value is typical for a bulk ion transport[29]. Hence, the calculated ionic conductivity can be ascribed to the bulk conductivity of the Ga0.15-LLZO phase and is comparable with the highest experimental and theoretical values previously reported[1,4,30]. Based on the capacitance value derived from the semicircle in the intermediate frequency range, 4.6×10^{-8} F cm^{-1}, the second R//CPE circuit can be

associated with inter-grain ion transport in the Ga0.15-LLZO pellet. This was confirmed by evaluating the impedance of the second semicircle with a pellet of the same material with different thicknesses. The impedance values for this process varied proportionally with the thickness of the pellet, which when corrected for by cell dimensions to give resistivity, gave a value with a variance of ≤5 % (Table S1), supporting the assigned process as being associated with grain boundary transport. The low-frequency semicircle has an associated capacitance of 8.8×10^{-5} F cm^{-2}. This value is in the range of a typical electrolyte/electrode interfacial response and can be attributed to the interfacial charge transfer of two symmetric interfaces with Li metal. The area specific charge transfer resistance, *ASR*, for this process is9.4 Ω cm^2. This is amongst the lowest values reported in the literature to-date for the interface between Li metal and garnet electrolytes, where the lowest values range between 1-2 Ω cm^2[31,32] and 58 Ω cm^2[30,33], generally using various surface modification techniques including the use of interlayers. In our case, we believe that the low value of *ASR* here is due to the clean and homogeneous surface as a result of the dry processing procedure adopted. The total conductivity of 8.2×10^{-4} S cm^{-1} was calculated from the sum of the resistances of the high and medium frequency equivalent circuits.

Chemical analysis using SIMS of the near-surface of the pristine garnet shows a slight reaction of Ga0.15-LLZO with (atmospheric) H_2O to form LiOH at the surface of the material (Figure 2), due to the brief exposure to ambient air during the transfer of the sample from the glove box to the SIMS chamber, seen in the elevated counts for Li$^+$, OH$^-$ and H$^-$ compared to the bulk (>0.1 μm, where the secondary ion signals are stable) in the SIMS depth profiles.

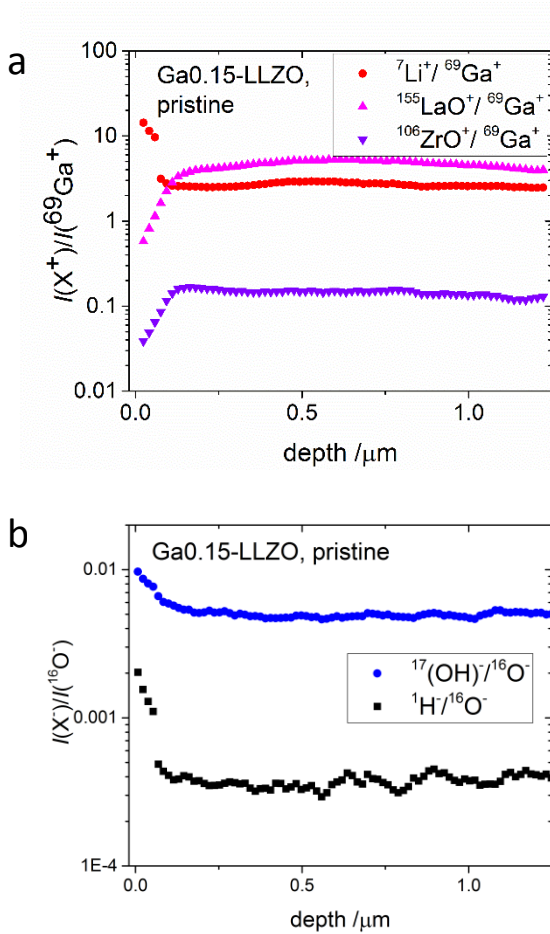**Figure 2.** FIB-SIMS depth profiles using a 590 pA primary ion beam current in pristine Ga0.15-LLZO; (a) positive secondary ions ^{7}Li$^+$, ^{155}(LaO)$^+$ and ^{106}(ZrO)$^+$ intensities I given as a ratio to the ^{69}Ga$^+$ intensity; (b) negative secondary ions ^{17}(OH)$^-$ and ^{1}H$^-$ intensities as a ratio of the ^{16}O$^-$ intensity.

This is expected to be absent in the samples measured with EIS, owing to the absence of air exposure and careful handling during cell setup and measurement. Surface roughness has an effect on the stabilisation of secondary ion signals, so to correct for this and changes in the sputter rate through altered layers of the garnet, the positive secondary ion intensities are given as a ratio to the ^{69}Ga$^+$ secondary ion intensity in Figure 2a. The ^{69}Ga$^+$ secondary ion intensity comprises of

contributions from both the primary ion beam of the instrument (the main contributor) and the gallium dopant in Ga0.15-LLZO. The negative secondary ion signals in Figure 2b are given as a ratio of $^{16}O^-$ intensity (which is stable in the bulk Ga0.15-LLZO) in order to profile the yield of protons from the OH^-/O^- ratio (see Experimental Section), and will be used in comparisons with moisture-exposed pellet profiles. Note that all analyses were performed within grains with no contributions from the grain boundaries, verified by visual inspection before and after depth-profiling using the high lateral resolution (5 nm) secondary electron and ion imaging modes in the FIB-SIMS, and have a depth resolution of 10-15 nm.

2.2. H_2O exposure and H^+/Li^+ exchange

The degradation of pristine Ga0.15-LLZO in air and in H_2O at 100 °C was followed for different periods of time using LEIS (Figure 3). LEIS is a surface technique sensitive to the uppermost atomic layer. Primary ions that penetrate past the immediate surface and are scattered by sub-surface atomic layers have a high probability for neutralisation and hence are not collected by the extraction field and are not detected.

To study atomic layers deeper into the sample an argon secondary sputtering ion gun is employed alternating with the primary one. Sputtering induces atomic mixing of the subsurface layers (~1 nm) and this leads to a reduction of the unique depth resolution of LEIS. Due to the absence of C signal, LiOH was assumed to be the primary component of the corrosion layer and so in order to study the depth of the LiOH corrosion layer, the oxygen intensity (which is normalised to the sum of all the surface species) was selected as a marker. In Figure 3 the x-axis represents the depth of the analysis in terms of the total argon sputtering dose; 0 ions/cm^2 corresponds to the sample surface.
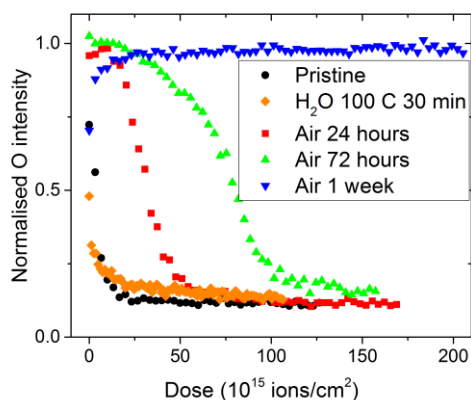
Figure 3. 3 keV ^{4}He LEIS depth profile with a 0.5 keV Ar sputter gun showing normalised oxygen intensities (with respect to the sum of all surface species) for Ga0.15-LLZO pellets following different atmospheric treatments.

The enhanced O signal after air exposure is due to LiOH at the surface which grows in thickness with exposure time. However, when the sample is exposed to deionised H_2O at 100 °C the layer is removed due to the dissolution of the LiOH degradation product under these aqueous conditions, and the normalized O intensity drops to its bulk value after a few sputter cycles (Figure 3). This cleaning effect was also proven by negative ion mass spectra taken from a rastered area of 100 μm by 100 μm of a pristine and a sample exposed to H_2O for 30 minutes at 100 °C (Figure S3), which showed a higher relative concentration of OH^- secondary ions in the pristine versus the water-immersed sample.

In order to probe the Li-ion dynamics modifications in the garnet structure due to the H^+/Li^+ exchange reaction, subsequent moisture reactions were performed by the immersion of the as-prepared, polished dry pellets in liquid H_2O heated to 100 °C on a hotplate for 5, 15 and 30 minutes.

Figure S2 shows the secondary electron and secondary positive ion images of all the pellets studied in this work. It can be seen that the garnet pellet maintains its mechanical integrity in liquid H_2O; however, areas which appear to be located along the grain boundaries appear darker in the electron images, suggesting a lower secondary electron yield in these regions after exposure to water. This will be correlated later in the paper to a three order of magnitude increment of the resistance in the grain boundaries upon reaction with H_2O.

On exposing the samples to liquid H_2O at 100 °C, the FIB-SIMS depth profiles (with an area of 7 μm by 7 μm, and therefore within-grain) shows four regions of differing secondary ion intensity and behaviour (Figure 4 and Figure S4). Figures 4a, b and c show a first region, up to about 0.15 μm depth in the 30 minutes H_2O-immersed sample, which can be described by high ion counts of Li^+, OH^- and H^- secondary ions. This first region is likely be caused by the front of the H^+/Li^+ exchange process and the formation of a thin corrosion layer of LiOH at the surface probably segregated during the transfer of the sample in air to the FIB-SIMS instrument. The second region between 0.15 and 1.35 μm (total thickness 1.2 μm) is a plateau region in the ratios for Li^+, H^- and OH^- secondary ions, indicating a region of equilibrated H^+ concentration, in the form of a stable H-Ga0.15-LLZO phase. At the edge of this region, from about 1 μm depth, the $Li^+/(Li^+$, bulk) ratio starts to gently rise, Figure 4c, showing a diffusion profile of Li from Ga0.15-LLZO into H-Ga0.15-LLZO. This continues until about 2 μm and is accompanied by decreasing OH^- and H^- counts (Figure 4a). We ascribe this observed behaviour to a chemical diffusion profile of protons into the bulk Ga0.15-LLZO. After 2 μm, flat profiles are seen for all species, indicating a region of unmodified, non-protonated Ga0.15-LLZO (with approaching-background values for OH^- and H^- counts). The corresponding profile of $Li^+/(Li^+$, bulk) for the pristine sample is shown in Figure

S5, showing a flat profile after an initial elevated ratio at the surface, due to the lack of exchange processes in the bulk material.
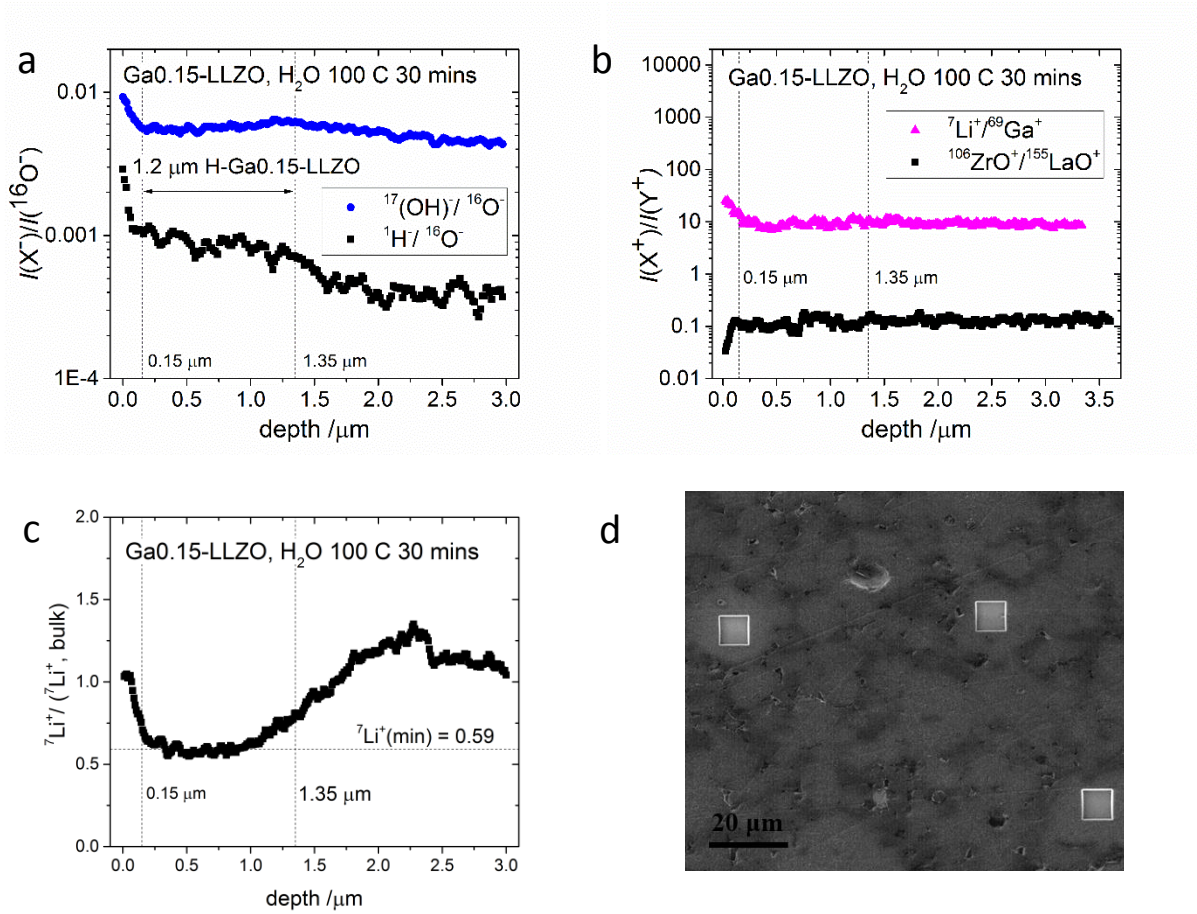

Figure 4. FIB-SIMS depth profiles with a 590 pA primary ion beam current on 30 minutes 100 °C H$_2$O-immersed Ga0.15-LLZO; (a) negative secondary ions ^{17}(OH)$^-$ and ^{1}H$^-$ intensities I as a ratio of ^{16}O$^-$ intensity; (b) positive secondary ions ^{7}Li$^+$ intensity as a ratio of ^{69}Ga$^+$ intensity and ^{106}(ZrO)$^+$ intensity as a ratio of ^{155}(LaO)$^+$ intensity; (c) ^{7}Li$^+$ intensity normalised to the intensity in the bulk (taken at end of depth profile); and (d) secondary electron images of craters for depth profiles, showing craters in the middle of the grains.

A schematic diagram of these regions is shown in Figure 5a, and depths for each region after different H_2O immersion times are summarised in Table 1. Figure 4a shows the ZrO^+/LaO^+ ratio taken for the depth profiles of the 30 minutes H_2O-immersed sample. It can be seen that the ZrO^+/LaO^+ ratio is stable with depth, indicating that there is no change in stoichiometry of the garnet following H_2O-immersion associated with the formation of the H-Ga0.15-LLZO phase.

Table 1. Overview of calculated values from the FIB-SIMS depth profiles for the H_2O-immersed samples at 100 °C.

	Ga0.15-LLZO H_2O 100 °C 5 minutes	Ga0.15-LLZO H_2O 100 °C 15 minutes	Ga0.15-LLZO H_2O 100 °C 30 minutes
Corrosion layer LiOH thickness [μm]	0.08+/- 0.02	0.15+/- 0.05	0.15+/- 0.05
H-Ga0.15-LLZO end depth [μm]	0.15+/- 0.02	0.87+/- 0.10	1.35+/- 0.10
H-Ga0.15-LLZO length [μm]	0.07+/- 0.04	0.72+/- 0.15	1.20+/- 0.15
OH^-, H^- background counts depth reached [μm]	1.0+/- 0.5	2.5+/- 0.5	3.0+/- 0.5
Diffusion length x of protons [μm]	0.85+/- 0.5	1.63+/- 0.6	1.65+/- 0.6

The possibility of a corrosion sub-product formation in the top 1 to 2 μm of the sample after 30 minutes H_2O exposure was also investigated with XRD on the spinning pellets. The sampling depth of X-ray diffraction is ~5 μm, and it is clear from the XRD pattern (Figure S6) that no further crystalline secondary phases exist, confirming that the cubic garnet structure is maintained following the H^+/Li^+ exchange. This is in agreement with previous reports of the stability of the cubic $Ia\overline{3}d$ phase following proton exchange[12,17]. Additionally, an increase in lattice parameter has

been observed following protonation, indicating exchange has occurred as reported by other authors due to a replacement of strong O-Li bonds with weaker O-H---O bonds[16,21]. A symmetry change to the non-centrosymmetric space group, $I\bar{4}3d$, as suggested by some authors for deep proton/lithium exchange and high temperature treatment[18,19], is not able to be verified here owing to the limitations of the quality of the diffraction data.

Increasing the immersion time in liquid H_2O at 100 °C leads to an increase in the thickness of the H-Ga0.15-LLZO region formed by H^+/Li^+ exchange, at least within the timescales of this experiment (Table 1). Immersion for 5 minutes in H_2O (Figure S4a) gives a H-Ga0.15-LLZO layer 0.07 μm thick. After 15 minutes exposure, this H-Ga0.15- LLZO region increases in length to 0.72 μm thickness (Figure S4b). After 30 minutes in H_2O, this increases further to 1.2 μm thickness (see Figure 4b). As previously mentioned, the diffusion tails in the negative ion profiles can be interpreted as the diffusion of protons into Ga0.15-LLZO, which are accompanied by a diffusion of lithium from the bulk through the H-Ga0.15-LLZO in the opposite direction to the protons. By normalising the OH^- and H^- secondary ion counts after the H^+/Li^+ exchange to their bulk values (taken as their value at the end of the depth profile), we can estimate the diffusion length of the protons within Ga0.15-LLZO by subtracting the beginnings of the diffusion tail (after the H-Ga0.15-LLZO region) from the depth at which the bulk (or 'background') OH^- or H^- counts are reached. The resulting diffusion lengths (x) are 0.85 μm, 1.63 μm and 1.65 μm, for 5, 15 and 30 minutes immersion (time t), respectively (Figure 5b), corresponding to a chemical diffusivity, $D_{chem}(H^+)$, of the order of 10^{-16} m^2s^{-1} at 100 °C in all three samples, using the relationship $x = 2\sqrt{(Dt)}$.

To summarise, H^+/Li^+ exchange occurs at the surface, resulting in the formation of LiOH corrosion layer products which are readily washed away in the water bath. This is followed by the

formation of a H-Ga0.15-LLZO region, followed by a region of Ga0.15-LLZO which contains a chemical diffusion profile of H^+ until the bulk, non-protonated Ga0.15-LLZO is reached. The stability of H-Ga0.15-LLZO at room temperature was measured after keeping the exchanged samples in a glove box for 8 weeks. Figure S7 shows that the H-Ga0.15-LLZO region extends to the same depth, indicating the stability and low proton diffusivity of this region for an extended period of time at room temperature in an argon atmosphere with <0.3 ppm H_2O (where no further reaction with H_2O can occur).
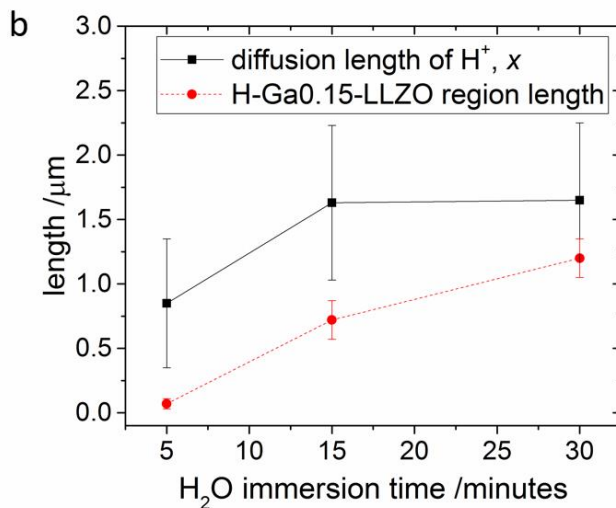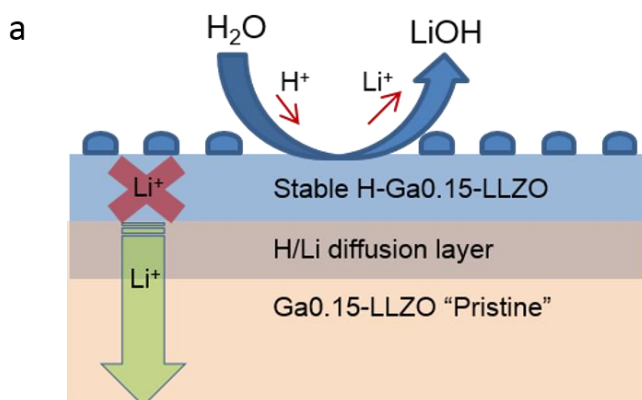

Figure 5. (a) Schematic of the surface composition of the garnet grain and evolution with depth; (b) Plot showing the length of the H-Ga0.15-LLZO region in the depth profiles (red dotted line) and the chemical diffusion length of H^+ (black full line).

2.4. Electrochemical Impedance Spectroscopy Results

The impedance spectra for the water-treated samples were measured with Li symmetric electrodes and compared with the spectrum of the pristine sample. Both the water-treated 15 minutes and 30 minutes samples display similar spectral forms to the pristine spectra (Figure 6), with three distinguishable semicircles which are fitted to parallel R//CPE elements, using the same equivalent circuit as in Figure 1, with a R_{int} of 5 Ω. Table 2 summarises the fitted components.
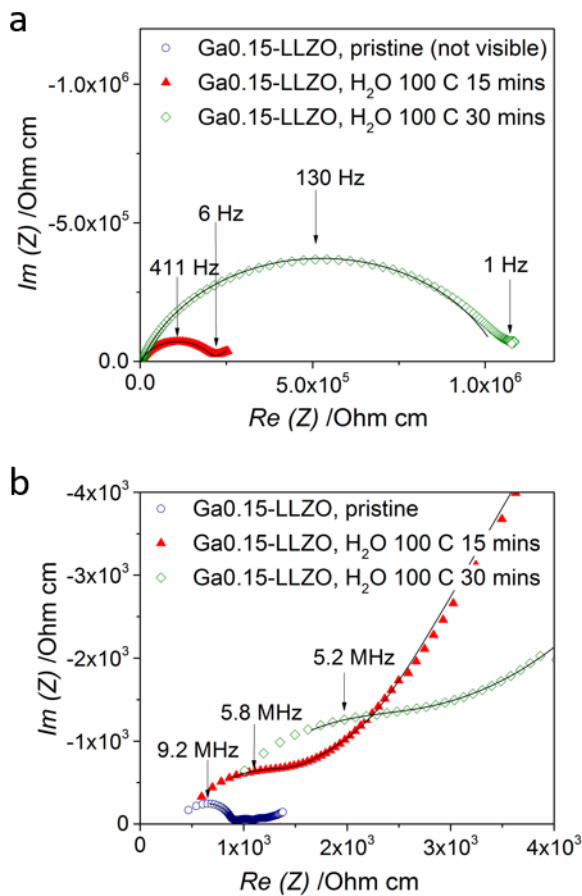

Figure 6. Nyquist plots measured at 25 ˚C for pristine and 100°C H_2O-immersed Ga0.15-LLZO pellets (15 minutes and 30 minutes immersion times), with symmetrical Li electrodes at lower (a) and high (b) frequency ranges.

Three clear trends can be observed:

1.   The apparent bulk ionic conductivity found from the R_1//CPE_1 (bulk transport) contribution decreases by one order of magnitude in the protonated samples. This is attributed to an additional resistance in series due to the formation of a protonated H-Ga0.15-LLZO layer with high resistivity (Figure 5a) which, although small in comparison to the total pellet thickness (~1 %), contributes heavily to an increase in the bulk resistance. It has been suggested that extensive proton-lithium exchange in LLZO would lead to a reduced Li^+ mobility as the mobile octahedral Li sites are depopulated[12,13,34]. It is important to note that the total bulk conductivity extracted from the

Table 2. Equivalent circuit model fits at 25 ˚C of impedance spectra parameters for pristine, 100 ˚C H_2O-immersed (15 and 30 minutes) Ga0.15-LLZO pellet cells with Li electrodes.

		Ga0.15-LLZO Pristine	Ga0.15-LLZO H_2O 100 °C 15 minutes	Ga0.15-LLZO H_2O 100 °C 30 minutes
R//CPE-1(bulk)	R_{bulk} x A/l [Ω cm]	8.6×10^2	1.8×10^3	2.4×10^3
	σ_{bulk} [S cm^{-1}]	1.2×10^{-3}	5.5×10^{-4}	4.1×10^{-4}
	C x l/A [F cm^{-1}]	3.7×10^{-11}	2.8×10^{-11}	9.8×10^{-11}
R//CPE-2 (grain boundary, GB)	R_{GB} x A/l [Ω cm]	3.5×10^2	2.1×10^5	5.0×10^5
	C x l/A [F cm^{-1}]	4.6×10^{-8}	9.0×10^{-10}	1.2×10^{-9}
R//CPE-3 (charge transfer, CT)	ASR (i.e. R_{CT} x $A/2$) [Ω cm^2]	9.4	2.4×10^3	-
	C/A [F cm^{-2}]	8.8×10^{-5}	8.7×10^{-5}	-
R//CPE-(1+2) (total)	R_{total} x A/l [Ω cm]	1.2×10^3	2.1×10^5	5.0×10^5
	σ_{total} [S cm^{-1}]	8.2×10^{-4}	4.8×10^{-6}	2.0×10^{-6}

protonated phases is on the order of magnitude of the most frequently reported values for garnet electrolytes in the literature, which could suggest a degree of facile proton-lithium exchange during processing and handling in these materials.

2. The apparent grain boundary resistance given by the R_2//CPE_2 contribution seems to be more heavily affected by the moisture reactivity. In this case, the resistance increases by three orders of magnitude following water treatment. Importantly, the impedance measurements in the pristine sample shows a lower grain boundary resistance than the bulk, indicating a higher Li mobility that could also be correlated to higher H^+/Li^+ exchange rates in the grain boundaries. In fact, the change in appearance of the grain boundaries in the electron and ion images after water treatment (Figures 4d and S2) indicate reactivity leading to a less conductive grain boundary, which is mirrored in the change in transport properties seen in EIS measurements. Shimonishi *et al.*[17] reported a similar decrease in grain boundary conductivity in LLZO pellets in H_2O at 50 °C, attributing the change to segregation of resistive decomposition products at the grain boundaries which were not detectable by XRD. The existence of a liquid phase sintering process leading to enriched Al and Li grain boundaries has been previously reported[35,36] and may be one of the factors contributing to higher reactivity towards proton-lithium exchange here.

3. The area specific resistance (*ASR*) for the charge transfer component (R_3//CPE_3) follows *ASR*(pristine) << *ASR*(H_2O, 15 minutes). The *ASR* in the pristine sample with Li electrodes is 9.4 Ω cm^2. The protonated sample after 15 minutes water treatment has an area specific resistance almost three orders of magnitude greater than the pristine, with a value of 2.4×10^3 Ω cm^2, indicating a large increase in the resistance at the H-Ga0.15-LLZO- Li metal interface. (The 30 minutes sample charge transfer component cannot be resolved as it occurs at too low frequencies at room temperature). Most reports to-date have focused on the presence of a corrosion layer of LiOH

and/or Li_2CO_3 following air exposure formed during the exchange process as the cause of increased interfacial resistance[23,24], which is generally recovered on mechanically abrading the corrosion layer[25]. For the first time, the effect of an extensively proton-rich, lithium-depleted LLZO surface on the interfacial properties with lithium metal electrodes is observed here (with a clean surface, free of LiOH and Li_2CO_3 species). The increased *ASR* following the proton-lithium exchange is most likely a result of decreased charge carrier mobility in this modified interfacial region. This behaviour is much more difficult to reverse with post-treatments, and represents a significant factor to consider when engineering interfaces of the LLZO electrolyte with lithium metal electrodes, with implications on cell performance such as fast charge/discharge cycles and preventing dendrite formation.

A closer look at the bulk resistance for the three samples, combined with the estimated H-Ga0.15-LLZO thickness as measured by FIB-SIMS depth profiling, can allow the approximate resistivity of the H-Ga0.15-LLZO material ($\rho_{\text{H-LLZO}}$) to be calculated. Figure S8 shows a schematic of the protonated region of the pellet under EIS measurements, with *l'* being the thickness of the H-Ga0.15-LLZO region in the protonated samples, and *l''* being the thickness of the unmodified, non-protonated Ga0.15-LLZO in these samples. In the pristine sample, R_{bulk}(pristine) is equal to 8.6×10^2 Ω cm, which allows the resistivity of the pristine Ga0.15-LLZO, ρ_{pristine}, to be found.

Using Equations 1 and 2,

$R_{\text{bulk}}(H_2O) = R_{\text{H-LLZO}}' + R_{\text{LLZO}}'' = 2l'/A\ \rho_{\text{H-LLZO}} + l''/A\ \rho_{\text{pristine}}$ (1)

$l'' = l-2l'$ (2)

where *l'* is taken from the FIB-SIMS depth profile measurements as the thickness of the H-Ga0.15-LLZO region (and *l* is the total thickness of the pellet), we find the resistivity of H-Ga0.15-LLZO

in both protonated samples (see Table S2 for details) to be: $\rho_{H\text{-}LLZO}(H_2O, 15\ minutes) = 1.2x10^5\ \Omega$ cm and $\rho_{H\text{-}LLZO}(H_2O, 30\ minutes) = 1.4x10^5\ \Omega$ cm.

This corresponds to bulk conductivities in the protonated garnets of $\sigma_{H\text{-}LLZO}(H_2O, 15\ minutes) = 8.6x10^{-6}\ S\ cm^{-1}$ at 25 ˚C and $\sigma_{H\text{-}LLZO}(H_2O, 30\ minutes) = 7.1x10^{-6}\ S\ cm^{-1}$ at 25 ˚C, which are almost three orders of magnitude lower than the pristine Ga0.15-LLZO ($\sigma_{LLZO,bulk}= 1.2x10^{-3}\ S\ cm^{-1}$). This low conductivity can be related to a very low ionic mobility in the protonated phase. The low Li mobility could be associated to a decrease in the Li charge carrier concentration and a concomitant change in conduction mechanism as suggested by previously reported *ab initio* studies[26]. However, further analysis should be performed to prove a change in the activation energy and evaluate possible cooperative effects of the H and Li charge carriers in these phases.

3. Conclusions

This study reveals the chemical and electrochemical effects of proton-lithium exchange in garnets on a macroscopic scale, correlating chemical changes due to the ion exchange with the change in bulk, grain boundary and interfacial ion transport in Ga-LLZO pellets with Li electrodes. Proton-lithium exchange was studied in the grains of $Li_{6.55}Ga_{0.15}La_3Zr_2O_{12}$ (Ga0.15-LLZO) pellets using FIB-SIMS depth profile analysis after immersing the pellets in liquid H_2O at 100 °C with varying timescales, ensuring the removal of water-soluble LiOH corrosion products. A protonated H-Ga0.15-LLZO layer was seen to form and increase in thickness with immersion times up to 30 minutes. This layer remained stable under the experimental conditions and for an extended period of time (8 weeks) in an argon atmosphere after quenching and drying to room temperature. The formation of a H-Ga0.15-LLZO region is accompanied by the appearance of a proton diffusion profile into the bulk Ga0.15-LLZO and a corresponding Li depletion profile.

Electrochemical impedance spectroscopy data showed a reduction in total conductivity from the pristine to the water-treated samples which has a calculated bulk resistivity of approximately 1×10^5 Ω cm in both 15 minute and 30 minute 100 ˚C H_2O-treated samples. This bulk resistivity is almost three orders of magnitude higher than in the pristine Ga0.15-LLZO with $R_{bulk}(pristine) = 8.6 \times 10^2$ Ω cm. A second semicircle component in the impedance spectra, $R_2//CPE_2$, was seen in all samples and attributed to a grain boundary contribution, which is shown to be very susceptible to moisture - after water bath treatment, the geometrically-corrected resistance R_{GB} for this component increases by three orders of magnitude to 5.0×10^5 Ω cm after 30 minutes H_2O immersion, suggesting a deeper degradation compared to the grains. The charge transfer resistance with Li electrodes dramatically increased (from 9.4 Ω cm^2 in the pristine to 2.4×10^3 Ω cm^2 in the 15 minutes immersed H_2O sample) after the proton exchange.

This study demonstrates the significant deterioration in the Li-ion mobilities of Li metal/Ga0.15-LLZO interfaces and in the bulk and grain boundaries upon reaction with H_2O due to the H^+/Li^+ exchange reaction. These findings highlight the link between proton-lithium exchange processes in lithium-conducting garnets and the impact on charge carrier transport, which have important implications on cell performance in lithium metal batteries using LLZO electrolytes.

4. Experimental Section

Synthesis, pellet preparation and characterisation:

The Ga0.15-LLZO (nominal composition $Li_{6.55}Ga_{0.15}La_3Zr_2O_{12}$) pellet samples in this work were prepared using a Pechini-type citrate/nitrate sol-gel route based on the process reported by Aguadero *et al.*[1] Stoichiometric amounts of lithium nitrate (99 %), lanthanum (III) nitrate hexahydrate (99.9 %), zirconium (IV) 2,4- pentanedionate and gallium (III) oxide (99.99 %) (all

Alfa Aesar) were dissolved in citric acid (10 wt%, equivalent to 0.542 M, approx. 200 ml, Sigma Aldrich) and a small amount of nitric acid to aid dissolution (68 wt%, approx. 5-10 ml, VWR Chemicals). An additional amount of lithium nitrate was added to allow for Li losses at elevated temperatures (nominally 10 wt% excess) and the solution was left to stir with a magnetic stirrer on a hotplate until a gel formed.

The gel was combusted in a furnace for 12 hrs at 600 °C (heating rate: 2 °C minute^{-1}, cooling rate: 10 °C minute^{-1}) in order to remove all water and organic compounds. The temperature was then held at 100 °C to prevent condensation of water and transferred to an argon-filled glove box (<0.3 ppm H_2O) via a vacuum antechamber. The white solid was hand-milled to a fine powder inside the glove box and calcined at 800 °C in dry flowing oxygen (99.9999 %; 0.5 ppm H_2O) for 12 hours. The subsequent powder was milled and pressed into pellets (8 mm diameter) in the glove box using a uniaxial press under 2 tonnes. The pellet was finally annealed under argon at 1150 °C for 6 hours (with a heating and cooling rate of 5 °C minute^{-1}), ensuring a bed of the same powder encased the pellet in the crucible, using a furnace coupled to the glove box.

A Bruker D2 Phaser and PANalytical X'Pert MR/PD diffractometer with nickel filtered copper *Kα* radiation (λ_{avg} = 1.5418 Å) was used to acquire X-ray diffraction patterns of the samples. Scanning electron microscope secondary electron images were recorded on Zeiss Sigma 300 scanning electron microscope with an electron beam energy of 5 keV.

Electrochemical tests:

Electrochemical impedance spectroscopy (EIS) AC measurements were performed using a Solatron 1260 Impedance Analyser in the frequency range of 7 MHz to 1 Hz at 25 °C with a signal amplitude of 100 mV. The garnet pellets were polished to 4000 grit with SiC abrasive inside the glove box. To prepare symmetric cells, lithium metal was scratched to remove any oxidized

surface, cut into disc shapes and pressed onto each side of the Ga0.15-LLZO pellet (without heating). This assembled stack was placed in a coin cell setup, using stainless steel spacers to ensure good electrode-electrolyte contact, and left to stabilise at room temperature for 24 hours to equilibrate the metal-electrolyte interface. The EIS data were analysed using Z-View software. The impedance spectra were fitted with an equivalent circuit consisting of a resistor in series (R_{int}), found to be 5 Ω in the setup used here, and three parallel combinations of a resistor and a constant-phase element arranged in series (R_1//CPE_1, R_2//CPE_2 and R_3//CPE_3). For all Nyquist plots, a constant-phase element (CPE) was used to model the non-ideal capacitive behavior represented by depressed semi-circles. This deviation from an ideal R//C circuit was considered in the calculations of the capacitance values. The true (effective) capacitance (C) was extracted using the resistance (R) and the CPE parameters (α and Q) from Equation 3[37–39]:

$$C = R^{(1-\alpha)/\alpha} Q^{1/\alpha} \tag{3}$$

Proton exchange:

The Ga0.15-LLZO pellets (polished to 4000 grit SiC paper) were immersed in a liquid deionised water bath (resistance 18.2 MΩ cm at 20 °C) at 100 °C for 5, 15 and 30 minutes to study the proton-lithium exchange. After immersion the samples were quenched in water to room temperature and dried under dynamic vacuum for 10 minutes before transferring to the glove box prior to focused ion beam – secondary ion spectrometry (FIB-SIMS) analysis.

LEIS measurements:

A Qtac100 LEIS instrument from ION-TOF GmbH was employed for the LEIS measurements. This instrument can operate with different noble gases as analysis primary beam: He, Ar or Ne. In the analysis here presented a pure helium ion source at 3 keV was selected. The primary beam scanning area was maintained at 750 µm by 750 µm in each analysis. In this instrument the ion

beam is normal to the sample surface. Primary ions that are scattered through an angle of 145°

(±1°) are detected by a double toroidal analyser (DTA). To perform the LEIS depth profiling

analysis the primary He^+ beam was cycled with an Ar^+ sputtering beam with a pause of one second

between cycles. The sputter argon beam has an energy of 0.5 keV and is rastered on the sample

surface over an area of 1500 μm by 1500 μm. The He^+ 3 keV ion dose for the LEIS analysis was

approximately $7x10^{14}$ ions/cm^2 with a beam current of 5000 pA. Each Ar^+ 0.5 keV sputter cycle

dose was larger at ~ $3.4x10^{15}$ ions/cm^2 at a current of 100 nA. The energy range for the

backscattered helium ions for each analysis was constant between 800 and 2800 eV.

FIB-SIMS measurements:

An FEI FIB200-SIMS ion microscope was used to image the samples and record mass spectra

from the surface of the materials, and used in depth profiling mode to obtain chemical information

as a function of depth. The primary beam was a Ga^+ ion source at 30 keV incident at 30° to the

normal of the ceramic surface operated with a range of currents from 30 pA for imaging and 590

pA for depth profiling. Simultaneous negative and positive secondary ions were detected in

dynamic SIMS mode (> 10^{14} particles cm^{-2} incident on the sample) using both FEI and Hiden EQS

quadrupole detectors. The FIB-SIMS instrument is equipped with detectors for secondary

electrons, positive ions and negative ions to allow an asynchronous semi-simultaneous signal

acquisition[28]. The crater depth was calibrated from the SEM image recorded with the sample tilted

at 45°.

Transfer of the pre-mounted samples was done by sealing the samples in a container in the glove

box, and transferring to the SIMS chamber before immediately pumping down to high vacuum

(>10^{-6} mbar). This meant that the samples for analysis were exposed to ambient air for a matter of

no more than a few minutes.

In the proton exchange experiments, OH^- and H^- secondary ions were used to characterise diffusion profiles as an indicator of H^+ diffusion into the garnets. The intensity ratio (OH^- / O^-) enables the diffusant concentration of protons to be profiled since the yield of O^- in the Ga0.15-LLZO matrix is expected to be constant. LaO^+ secondary ions were profiled as a high intensity marker of the corresponding Ga0.15-LLZO matrix species. To correct for changes in sputter rate resulting from sputtering through modified layers in the garnet, the positive ions intensities can be given as a ratio to the $^{69}Ga^+$ signal. The $^{69}Ga^+$ signal comprises of contributions from both the primary beam of the instrument (the main contributor) and the gallium dopant in the Ga0.15-LLZO.

Reference signals for all secondary ions followed were established by collecting depth profiles and mass spectra on a pristine Ga0.15-LLZO reference with each analysis session using the same conditions. The 'bulk' unmodified, non-protonated Ga0.15-LLZO secondary ion counts in the water-treated samples (at the end of the depth profiles) were thus verified to be below reference levels of H^- and OH^- in the pristine sample and could be thus used as internal standards for unprotonated Ga0.15-LLZO within the depth profiles. The FIB-SIMS instrument under the conditions used here has a sub- 100 nm lateral resolution (~5 nm in imaging mode with 30 pA beam current); sub- 20 nm depth resolution (10-15 nm at 500 pA primary beam current for the depth profiles). The minimum increment is 0.05 *amu* for the quadrupole SIMS detectors where the full width, half-maximum value for a typical $^{16}O^-$ peak is 0.37 *amu.*

ASSOCIATED CONTENT

Supporting Information. XRD patterns and SEM images of pristine and water-immersed Ga0.15-LLZO; surface SIMS spectra of pristine and 100 °C 30 minutes H_2O-immersed Ga0.15-LLZO; negative SIMS depth profiles of 5 and 15 minutes H_2O-immersed Ga0.15-LLZO; table of normalized thicknesses and impedance values for pristine pellet; SIMS depth profiles before and after 8 weeks water immersion; schematic of thicknesses in corroded pellet; table of resistivity calculations. This material is available free of charge via the Internet at http://pubs.acs.org.

AUTHOR INFORMATION

Corresponding Author

*a.aguadero@imperial.ac.uk

Author Contributions

The manuscript was written through contributions of all authors. All authors have given approval to the final version of the manuscript.

ABBREVIATIONS

AC, alternating current; ASR, area specific resistance; CPE, constant phase element; DTA, double toroidal analyser; EIS, electrochemical impedance spectroscopy; FIB-SIMS, focused ion beam-SIMS; LEIS, low energy ion scattering; LLZO, $Li_7La_3Zr_2O_{12}$; SEM, scanning electron microscopy; SIMS, secondary ion mass spectrometry; XRD, X-ray diffraction.

REFERENCES

(1)   Bernuy-Lopez, C.; Manalastas, W.; Miguel, J.; Aguadero, A.; Aguesse, F.; Kilner, J. A. Atmosphere Controlled Processing of Ga-Substituted Garnets for High Li-Ion Conductivity Ceramics. *Chem. Mater.* **2014**, *26*, 3610–3617.

(2)   El Shinawi, H.; Janek, J. Stabilization of Cubic Lithium-Stuffed Garnets of the Type "Li$_7$La$_3$Zr$_2$O$_{12}$" by Addition of Gallium. *J. Power Sources* **2013**, *225*, 13–19.

(3)   Rettenwander, D.; Geiger, C. A.; Tribus, M.; Tropper, P.; Amthauer, G. A Synthesis and Crystal Chemical Study of the Fast Ion Conductor Li$_{7-3x}$Ga$_x$La$_3$Zr$_2$O$_{12}$ with x = 0.08 to 0.84. *Inorg. Chem.* **2014**, *53*, 6264–6269.

(4)   Jalem, R.; Rushton, M.; Manalastas, W.; Nakayama, M.; Kasuga, T.; Kilner, J. A.; Grimes, R. W. Effects of Gallium Doping in Garnet-Type Li$_7$La$_3$Zr$_2$O$_{12}$ Solid Electrolytes. *Chem. Mater.* **2015**, *27*, 2821–2831.

(5)   Ma, C.; Cheng, Y.; Yin, K.; Luo, J.; Sharafi, A.; Sakamoto, J.; Li, J.; More, K. L.; Dudney, N. J.; Chi, M. Interfacial Stability of Li Metal-Solid Electrolyte Elucidated via in Situ Electron Microscopy. *Nano Lett.* **2016**, *16*, 7030–7036.

(6)   Cheng, L.; Chen, W.; Kunz, M.; Persson, K.; Tamura, N.; Chen, G.; Doeff, M. Effect of Surface Microstructure on Electrochemical Performance of Garnet Solid Electrolytes. *ACS Appl. Mater. Interfaces* **2015**, *7*, 2073–2081.

(7)   Sudo, R.; Nakata, Y.; Ishiguro, K.; Matsui, M.; Hirano, a.; Takeda, Y.; Yamamoto, O.; Imanishi, N. Interface Behavior between Garnet-Type Lithium-Conducting Solid Electrolyte and Lithium Metal. *Solid State Ionics* **2014**, *262*, 151–154.

(8)   Aguesse, F.; Manalastas, W.; Buannic, L.; Lopez del Amo, J. M.; Singh, G.; Llordes, A.; Kilner, J. A. Investigating the Dendritic Growth during Full Cell Cycling of Garnet Electrolyte in Direct Contact with Li Metal. *ACS Appl. Mater. Interfaces* **2017**, *9*, 3808–3816.

(9)   Orera, A.; Larraz, G.; Rodríguez-Velamazán, J. A.; Campo, J.; Sanjuán, M. L. Influence of Li^+ and H^+ Distribution on the Crystal Structure of $Li_{7-x}H_xLa_3Zr_2O_{12}$ ($0 \leq x \leq 5$) Garnets. *Inorg. Chem.* **2016**, *55*, 1324–1332.

(10)   Liu, C.; Rui, K.; Shen, C.; Badding, M. E.; Zhang, G.; Wen, Z. Reversible Ion Exchange and Structural Stability of Garnet-Type Nb-Doped $Li_7La_3Zr_2O_{12}$ in Water for Applications in Lithium Batteries. *J. Power Sources* **2015**, *282*, 286–293.

(11)   Slater, P. R.; Greaves, C. The Ionic Conductivity of Proton Containing Garnets and their Decomposition Products. *Solid State Ionics* **1992**, *53–56*, 989–992.

(12)   Ma, C.; Rangasamy, E.; Liang, C.; Sakamoto, J.; More, K. L.; Chi, M. Excellent Stability of a Lithium-Ion-Conducting Solid Electrolyte upon Reversible Li^+/H^+ Exchange in Aqueous Solutions. *Angew. Chem. Int. Ed. Engl.* **2015**, *54*, 129–133.

(13)   Orera, A.; Larraz, G.; Rodríguez-Velamazán, J. A.; Campo, J.; Sanjuán, M. L. Influence of Li^+ and H^+ Distribution on the Crystal Structure of $Li_{7-x}H_xLa_3Zr_2O_{12}$ ($0 \leq x \leq 5$) Garnets. *Inorg. Chem.* **2016**, *55,* 1324-1332.

(14)   Galven, C.; Fourquet, J.-L. Instability of the Lithium Garnet $Li_7La_3Sn_2O_{12}$: Li^+/H^+ Exchange and Structural Study. *Chem. Mater.* **2011**, *23*, 1892–1900.

(15)   Nyman, M.; Alam, T. M.; McIntyre, S. K.; Bleier, G. C.; Ingersoll, D. Alternative Approach

to Increasing Li Mobility in Li-La-Nb/Ta Garnet Electrolytes. *Chem. Mater.* **2010**, *22*, 5401–5410.

(16) Galven, C.; Dittmer, J.; Suard, E.; Le Berre, F.; Crosnier-Lopez, M.-P. Instability of Lithium Garnets against Moisture. Structural Characterization and Dynamics of $Li_{7-x}H_x La_3Sn_2O_{12}$ and $Li_{5-x}H_xLa_3Nb_2O_{12}$. *Chem. Mater.* **2012**, *24*, 3335–3345.

(17) Shimonishi, Y.; Toda, A.; Zhang, T.; Hirano, A.; Imanishi, N.; Yamamoto, O.; Takeda, Y. Synthesis of Garnet-Type $Li_{7-x}La_3Zr_2O_{12-1/2x}$ and Its Stability in Aqueous Solutions. *Solid State Ionics* **2011**, *183*, 48–53.

(18) Sanjuán, M. L.; Orera, A.; Sobrados, I.; Fuentes, A. F.; Sanz, J. Structural Transition in Orthorhombic $Li_{5-x}H_xLa_3Nb_2O_{12}$ Garnets Induced by a Concerted Lithium and Proton Diffusion Mechanism. *J. Mater. Chem. A* **2018**, *6*, 2708–2720.

(19) Galven, C.; Suard, E.; Mounier, D.; Crosnier-Lopez, M.-P.; Le Berre, F. Structural Characterization of a New Acentric Protonated Garnet: $Li_{6-x}H_xCaLa_2Nb_2O_{12}$. *J. Mater. Res.* **2013**, *28*, 2147–2153.

(20) Xia, W.; Xu, B.; Duan, H.; Tang, X.; Guo, Y.; Kang, H.; Li, H.; Liu, H. Reaction Mechanisms of Lithium Garnet Pellets in Ambient Air: The Effect of Humidity and CO_2. *J. Am. Ceram. Soc.* **2017**, *100*, 2832–2839.

(21) Yow, Z. F.; Oh, Y. L.; Gu, W.; Rao, R. P.; Adams, S. Effect of Li^+/H^+ Exchange in Water Treated Ta-Doped $Li_7La_3Zr_2O_{12}$. *Solid State Ionics* **2016**, *292*, 122–129.

(22) Aguesse, F.; López del Amo, J. M.; Roddatis, V.; Aguadero, A.; Kilner, J. A. Enhancement of the Grain Boundary Conductivity in Ceramic $Li_{0.34}La_{0.55}TiO_3$ Electrolytes in a Moisture-

Free Processing Environment. *Adv. Mater. Interfaces* **2014**, *1*, 1300143.

(23)   Cheng, L.; Wu, C. H.; Jarry, A.; Chen, W.; Ye, Y.; Zhu, J.; Kostecki, R.; Persson, K.; Guo, J.; Salmeron, M.; Chen, G.; Doeff, M. Interrelationships among Grain Size, Surface Composition, Air Stability, and Interfacial Resistance of Al-Substituted $Li_7La_3Zr_2O_{12}$ Solid Electrolytes. *ACS Appl. Mater. Interfaces* **2015**, *7*, 17649–17655.

(24)   Sharafi, A.; Yu, S.; Naguib, M.; Lee, M.; Ma, C.; Meyer, H. M.; Nanda, J.; Chi, M.; Siegel, D. J.; Sakamoto, J. Impact of Air Exposure and Surface Chemistry on $Li–Li_7La_3Zr_2O_{12}$ Interfacial Resistance. *J. Mater. Chem. A* **2017**, *5*, 13475–13487.

(25)   Cheng, L.; Crumlin, E. J.; Chen, W.; Qiao, R.; Hou, H.; Franz Lux, S.; Zorba, V.; Russo, R.; Kostecki, R.; Liu, Z.; Persson, K.; Yang, W.; Cabana, J.; Richardson, T.; Chen, G.; Doeff, M. The Origin of High Electrolyte–Electrode Interfacial Resistances in Lithium Cells Containing Garnet Type Solid Electrolytes. *Phys. Chem. Chem. Phys.* **2014**, *16*, 18294.

(26)   Xu, M.; Park, M. S.; Lee, J. M.; Kim, T. Y.; Park, Y. S.; Ma, E. Mechanisms of Li^+ Transport in Garnet-Type Cubic $Li_{3+x}La_3M_2O_{12}$ (M = Te, Nb, Zr). *Phys. Rev. B - Condens. Matter Mater. Phys.* **2012**, *85*, 1–5.

(27)   Li, Y.; Han, J.-T.; Wang, C.-A.; Xie, H.; Goodenough, J. B. Optimizing Li^+ Conductivity in a Garnet Framework. *J. Mater. Chem.* **2012**, *22*, 15357.

(28)   Chater, R. J.; Smith, A. J.; Cooke, G. Simultaneous Detection of Positive and Negative Secondary Ions. *J. Vac. Sci. Technol. B* **2016**, *34*, 3–122.

(29)   Irvine, J. T. S.; Sinclair, D. C.; West, A. R. Electroceramics Characterization by Impedance Spectroscopy. *Adv. Mater.* **1990**, *2*, 132–138.

(30) Rettenwander, D.; Redhammer, G.; Preishuber-Pflügl, F.; Cheng, L.; Miara, L.; Wagner, R.; Welzl, A.; Suard, E.; Doeff, M. M.; Wilkening, M.; Fleig, J.; Amthauer, G. Structural and Electrochemical Consequences of Al and Ga Cosubstitution in $Li_7La_3Zr_2O_{12}$ Solid Electrolytes. *Chem. Mater.* **2016**, *28*, 2384–2392.

(31) Sharafi, A.; Kazyak, E.; Davis, A. L.; Yu, S.; Thompson, T.; Siegel, D. J.; Dasgupta, N. P.; Sakamoto, J. Surface Chemistry Mechanism of Ultra-Low Interfacial Resistance in the Solid-State Electrolyte $Li_7La_3Zr_2O_{12}$. *Chem. Mater.* **2017**, *29*, 7961–7968.

(32) Han, X.; Gong, Y.; Fu, K.; He, X.; Hitz, G. T.; Dai, J.; Pearse, A.; Liu, B.; Wang, H.; Rubloff, G.; Mo, Y.; Thangadurai, V.; Wachsman, E. D.; Hu, L. Negating Interfacial Impedance in Garnet-Based Solid-State Li Metal Batteries. *Nat. Mater.* **2017**, *16*, 572-579.

(33) Tsai, C.-L.; Roddatis, V.; Vinod Chandran, C.; Ma, Q.; Uhlenbruck, S.; Bram, M.; Heitjans, P.; Guillon, O. $Li_7La_3Zr_2O_{12}$ Interface Modification for Li-Dendrite Prevention. *ACS Appl. Mater. Interfaces* **2016**, *8*, 10617–10628.

(34) Larraz, G.; Orera, A.; Sanz, J.; Sobrados, I.; Diez-Gómez, V.; Sanjuán, M. L. NMR Study of Li Distribution in $Li_{7-x}H_xLa_3Zr_2O_{12}$ Garnets. *J. Mater. Chem. A* **2015**, *3*, 5683–5691.

(35) Kumazaki, S.; Iriyama, Y.; Kim, K.-H.; Murugan, R.; Tanabe, K.; Yamamoto, K.; Hirayama, T.; Ogumi, Z. High Lithium Ion Conductive $Li_7La_3Zr_2O_{12}$ by Inclusion of both Al and Si. *Electrochem. commun.* **2011**, *13*, 509–512.

(36) Hubaud, A. A.; Schroeder, D. J.; Key, B.; Ingram, B. J.; Dogan, F.; Vaughey, J. T. Low Temperature Stabilization of Cubic $(Li_{7-x}Al_{x/3})La_3Zr_2O_{12}$: Role of Aluminum during Formation. *J. Mater. Chem. A* **2013**, *1*, 8813-8818.

(37)   McNealy, B. E.; Hertz, J. L. On the Use of the Constant Phase Element to Understand Variation in Grain Boundary Properties. *Solid State Ionics* **2014**, *256*, 52–60.

(38)   Hirschorn, B.; Orazem, M. E.; Tribollet, B.; Vivier, V.; Frateur, I.; Musiani, M. Determination of Effective Capacitance and Film Thickness from Constant-Phase-Element Parameters. *Electrochim. Acta* **2010**, *55*, 6218–6227.

(39)   Brug, G. J.; van den Eeden, A. L. G.; Sluyters-Rehbach, M.; Sluyters, J. H. The Analysis of Electrode Impedances Complicated by the Presence of a Constant Phase Element. *J. Electroanal. Chem.* **1984**, *176*, 275–295.

(40)   Zhu, Y.; He, X.; Mo, Y. Origin of Outstanding Stability in the Lithium Solid Electrolyte Materials: Insights from Thermodynamic Analyses Based on First-Principles Calculations. *ACS Appl. Mater. Interfaces* **2015**, *7*, 23685–23693.

TOC: